Structural TEM study of nonpolar *a*-plane gallium nitride grown on (11$\underline{2}$0) 4H-SiC by organometallic vapor phase epitaxy.

Dmitri N. Zakharov and Zuzanna Liliental-Weber

Lawrence Berkeley National Laboratory, Materials Sciences Division, 1 Cyclotron Rd., M/S 62-203, Berkeley, CA 94720-8253

Brian Wagner, Zachary J. Reitmeier, Edward A. Preble, and Robert F. Davis

North Carolina State University, Materials Science and Engineering Department, 2401 Stinson Dr., Raleigh, NC 27695-7907

ABSTRACT

Conventional and high resolution electron microscopy have been applied for studying lattice defects in nonpolar a-plane GaN grown on a 4H-SiC substrate with an AlN buffer layer. Samples in plan-view and cross-section configurations have been investigated. Basal and prismatic stacking faults together with Frank and Shockley partial dislocations were found to be the main defects in the GaN layers. High resolution electron microscopy in combination with image simulation supported Drum's model for the prismatic stacking faults. The density of basal stacking faults was measured to be $\sim 1.6 \times 10^6 \text{cm}^{-1}$. The densities of partial dislocations terminating I_1 and I_2 types of intrinsic basal stacking faults were $\sim 4.0 \times 10^{10} \text{cm}^{-2}$ and $\sim 0.4 \times 10^{10} \text{cm}^{-2}$, respectively. The energy of the I_2 stacking fault in GaN was estimated to be (40 ± 4) erg/cm^2 based on the separation of Shockley partial dislocations. To the best of our knowledge, the theoretically predicted I_3 basal stacking fault in GaN was observed experimentally for the first time.

[a] Correspondence author; e-mail: dnzakharov@lbl.gov

I. INTRODUCTION

Wurtzite III-nitride heterostructures, have been shown to be promising materials for laser and light emitting diodes. They are usually grown on (0001) Al_2O_3, 6H-SiC or free-standing GaN substrates.[1-3] In devices based on such materials, active GaN-based heterostructural epilayers have the polar c-axis of the hexagonal structure perpendicular to the sample surface and to the interfaces of the active layers. This orientation causes spontaneous and piezoelectric polarizations within the active layers aligned along the polar c-axis, which result in high interface charge densities and spatial separation of the electron and hole wave functions, red-shifting the photoluminescence peak and decreasing the peak intensity.[4-6] One of the possible solutions to eliminate these undesirable effects is to grow GaN-based epilayers in nonpolar orientations. Recently, nonpolar m-plane and a-plane GaN/AlGaN multiple quantum well structures have been grown on (100) γ-LiAlO$_2$ and (1$\underline{1}$02) r-plane Al_2O_3 substrates, respectively. These layers show a lack of red shift and an improved photoluminescence intensity.[7-10] Investigations of similar layers by transmission electron microscopy revealed high densities of basal stacking faults and threading dislocations.[11, 12]

(11$\underline{2}$0) 4H-SiC is an alternative substrate suitable for a-plane GaN-based layer growth. In this paper growth of a-plane GaN layers on the (11$\underline{2}$0) surface of a 4H-SiC substrate by organometallic vapor phase epitaxy is reported. Because the optoelectronic properties of the layers depend on structural quality, systematic studies of the layers grown in the non-polar direction were performed by conventional and high resolution electron microscopy.

II. DEFECTS IN THE WURTZITE STRUCTURE

GaN exists in two different polytypes, namely wurtzite and sphalerite. The wurtzite structure consists of two hexagonal close-packed sublattices (Ga and N) shifted by 0.377c along [0001]. In both sublattices (0002) planes are close-packed. Stacking these basal (0002)

planes in the …AαBβAαBβAαBβ… sequence forms the wurtzite structure, in which the atoms are tetrahedrally coordinated. Here capital letters correspond to Ga layers and the Greek letters to N layers. For simplicity the GaN molecule can be taken as a stacking unit. In this case the Greek letters can be omitted. Thus the hexagonal stacking sequence will further be referred to as …ABABAB…, where capital letters represent Ga-N atomic bilayers. In the above notation the sphalerite structure can be represented as an …ABCABCABC… stacking sequence along the [111] direction.

Basal plane stacking faults (BSF) in the wurtzite structure can be treated as planar defects forming locally the ABC cubic structure within the usual …ABABAB… stacking sequence. Three types of BSFs can exist in a wurtzite structure: two intrinsic (I_1 and I_2) and one extrinsic (E).[13] The I_1 type BSF is formed either by removal or insertion of a basal plane with further $1/3<1\underline{1}00>$ slip of one part of a crystal with respect to the other to decrease the fault energy. This changes the perfect stacking sequence of …ABABABAB… to one with …ABAB**ABC**BCBC… [Fig. 1(a)]. The single cubic stacking ABC is underlined. Such a fault has to be bounded by a sessile Frank-Shockley dislocation with Burgers vector $\boldsymbol{b}=1/6<20\underline{2}3>$. The I_2 type fault having the …ABAB**ABCA**CACA… [Fig. 1(b)] stacking sequence can be formed by $1/3<1\underline{1}00>$ shear of one part of a crystal with respect to the other or by dissociation of a perfect dislocation ($\boldsymbol{b}=1/3<11\underline{2}0>$) into two Shockley partials with $\boldsymbol{b}=1/3<1\underline{1}00>$. The E type BSF with a stacking sequence …ABAB**ABCAB**ABAB… [Fig. 1(c)] appears due to insertion of an extra basal plane. This type of fault is bounded by Frank partials with $\boldsymbol{b}=1/2[0001]$.

The energy of BSFs γ is proportional to the number of cubic bilayers in the particular fault. As described I_1, I_2 and E type defects consist of one, two and three cubic bilayers, respectively, and their energy to a first approximation is $\gamma_E \approx \frac{3}{2}\gamma_{I_2} \approx 3\gamma_{I_1}$. Although the I_1

type BSF has the lowest energy, its formation requires removal of a basal bilayer in addition to the basal shear of $1/3<1\underline{1}00>$. This means that the I_1 BSF likely to be formed during the growth process. Deformation caused by stress during or after growth can cause formation of the I_2 type BSF by movement of a glissile Shockley partial dislocation in the basal plane. The E type BSF is formed by precipitation of point defects on the basal plane forming a dislocation loop. Such a loop results in a high-energy fault. Thus the basal shear is likely to happen in order to reduce the fault energy. If the basal shear occurs it produces an I_1 type BSF for an interstitial, as well as for a vacancy loop.[14]

One more type of intrinsic BSF in which one of the A or B bilayers occupies the 'wrong' C position was predicted theoretically by C. Stampfl and C. G. Van de Walle.[15] Such a fault would, for example, have a stacking sequence …ABAB**ABCBA**BAB… [Fig. 1(d)]. The authors calculated that this fault would have the second-lowest formation energy after I_1.

Stacking faults are also possible on planes other than the *c*-plane. Faults formed on prismatic $\{1\underline{2}10\}$ planes were first identified by Drum[16] in AlN crystals [Fig. 2(a)]. From the diffraction conditions under which defect contrast vanishes in TEM micrographs it was deduced that these prismatic stacking faults (PSFs) on the $(1\underline{2}10)$ plane have the fault vector $R=1/2[10\underline{1}1]$. PFSs were found to terminate BSFs. Stair-rod dislocations were observed at the intersections of PSFs and BSFs, since the intersecting faults had different fault vectors. The faults on prismatic planes in wurtzite ZnS have been reported by Amelinckx's group.[14] The structural model of these defects, often called in the literature a stacking mismatch boundary (SMB) with $R=1/6[20\underline{2}3]$, has been proposed[14], as shown in Fig. 2(b). It was noted that SMBs never end inside the crystal but rather constitute folded arrangements with BSFs. In this case stair-rod dislocations are not observed because SMBs have the same fault vectors as BSFs. High resolution electron microscopy studies of AlN and AlGaN layers grown on (0001) 6H-SiC and sapphire substrates[17, 18] showed that more than 90% of the faults formed on prismatic

planes had the structure proposed by Drum.[16] Calculations of atomic structure for PSFs indicated that there are no wrong or broken bonds, but due to large distortions from the tetrahedral bonding the formation energy was estimated to be 72 meV/Å^2 (i.e. 1153 erg/cm^2).[19] It was found that the PSF model proposed by Drum[16] is energetically more favorable than the SMB model proposed by Amelinckx.[14]

III. EXPERIMENT

The AlN buffer layer and the GaN epilayer were sequentially grown on a 12mm x 12mm square 4H-SiC (11$\underline{2}$0) substrate in a cold-walled, vertical, pancake-style organometallic vapor phase epitaxy (OMVPE) system. The 100 nm thick AlN buffer layer and the 1μm thick undoped GaN layer were grown at 20 Torr at temperatures of 1100°C and 1015°C, respectively. The precursor species of Tri-methylaluminum, Tri-ethylgallium and Ammonia with mass flow rates of 5.4 μmol/min, 101 μmol/min and 0.14 mol/min, respectively were mixed with high purity H_2 (3 slm) in a two-inch internal diameter sleeve located two inches above the substrate.

Samples were studied by conventional transmission electron microscopy (TEM) and high resolution electron microscopy (HREM) using JEOL 3010 and JEOL ARM microscopes operated at 300kV and 800kV respectively. The JEOL 3010 and the JEOL ARM microscopes had point-to-point resolutions of 2.1Å and 1.5Å respectively and a tilting capability ±40º. Other microscope parameters were as follows: spherical aberration C_s=1.4mm and C_s=2.0mm, chromatic aberration C_c=2.2mm and C_c=3.0mm, spread of focus ~100Å and ~120Å, beam convergence angle ~0.65mrad and ~0.85mrad, and Scherzer defocus -63.5nm and -52.5nm respectively. Cross-sectional and plan-view samples for these studies were prepared by mechanical polishing followed by dimpling down to 10μm and Ar ion milling at 5kV until perforation occurred.

HREM images were recorded near Scherzer defocus in order to compare them with simulated ones. Crystal kit and MacTempas software were used for high resolution image simulation utilizing the multislice method.[20] Tables of HREM images including defocus vs. thickness were calculated in order to obtain the best matching with the experimental images.

IV. RESULTS AND DISCUSSION

A. Epitaxial relationships

The epitaxial relationships between the deposited GaN/AlN layers and 4H-SiC substrate were studied by cross-sectional TEM. Selected area electron diffraction patterns recorded at the [1$\underline{1}$00] zone axis show that the AlN and GaN layers have the same orientation as the substrate. Epitaxial relationships can be written as follows: (11$\underline{2}$0) GaN || (11$\underline{2}$0) AlN || (11$\underline{2}$0) 4H-SiC and [1$\underline{1}$00] GaN || [1$\underline{1}$00] AlN || [1$\underline{1}$00] 4H-SiC [Fig. 3].

B. Basal stacking faults and dislocation density

A bright field image of a cross-sectional sample [Fig. 4(a)] recorded for two beam conditions with **g**-vector 11$\underline{2}$0 close to the [1$\underline{1}$00] zone axis shows dislocations with Burgers vector components parallel to [11$\underline{2}$0]. These are partial dislocations with **b**=1/3[10$\underline{1}$0] and **b**=1/3[01$\underline{1}$0] terminating BSFs. In order to bring BSFs into strong contrast it is necessary to tilt the specimen in the *c*-plane by +30º or -30º from [1$\underline{1}$00] towards [$\underline{2}$110] or [1$\underline{2}$10] zone axis, respectively, so that **g**=$\underline{1}$010. For the image obtained under the **g**=$\underline{1}$010 diffraction condition [Fig. 4(b)] the contrast typical for BSFs (defects arranged perpendicular to the substrate) is clearly seen. The majority of BSFs are nucleated at the 4H-SiC/AlN interface and propagate through the AlN and the GaN layers to the sample surface.

TEM (11$\underline{2}$0) plan-view samples have also been investigated in order to measure dislocation density. The plan-view configuration is also more suitable for HREM structural

studies of BSFs with the [11$\underline{2}$0] zone axis, since these defects are in edge-on configuration and tilting of the specimen by a large angle is not required. For this zone axis configuration BSFs are visible as thin lines parallel to c-planes of GaN when bright field images were obtained under a two beam condition with $\boldsymbol{g}$=1$\underline{1}$00 [Fig.5(a)]. The measured density of BSFs was ~1.6×10^{6}cm^{-1}. Such a high density of BSFs results in streaking of diffraction spots in the [0001] direction on selected area electron diffraction patterns recorded along the [11$\underline{2}$0] zone axis [Fig. 6(a)]. Some of the BSFs continue through the whole field of view, while others are terminated by partial dislocations. Some of such terminations are marked by black and white arrows [Fig. 5(a), (d) and (e)]. The image on Fig. 5(b), obtained under the two beam condition for $\boldsymbol{g}$=0002 is taken from the same area of the sample as the image on Fig. 5(a). Black and white arrows on Fig. 5(b) point to the same BSFs terminations as on Fig. 5(a). Stacking faults are out of contrast for two beam imaging conditions with $\boldsymbol{g}$=0002, therefore we can observe different contrast behavior of partial dislocations marked by black and white arrows. Namely, partial dislocations bounding BSFs marked with black arrows are in contrast on Fig. 5(b), whereas dislocations marked with white arrows are out of contrast on the same image [also see an enlargement on Fig. 5(g) and Fig. 5(h)]. Under the above imaging conditions one can draw a conclusion that two types of dislocations are present in the sample: the first one which has a component of Burgers vector parallel to [0001] (black arrows) and the second one which has no component of Burgers vector along [0001]. As it will be shown in the next paragraph the first type dislocations are bounding I_1 BSFs and the second type – I_2 BSFs. The densities of these dislocations are ~4.0×10^{10}cm^{-2} and ~0.4×10^{10}cm^{-2}, respectively.

Fig. 7 shows characteristic HREM images of BSFs revealed in the sample. According to the observed stacking sequences the first two images [Figs. 7(a) and 7(b)] represent I_1 type BSF with the sequences …ABAB**ABC**BCBC…and …ABA**BAC**ACAC… respectively. These I_1 type BSFs are formed due to removal [Fig. 7(a)] or insertion [Fig. 7(b)] of a basal

plane followed by 1/3[1$\underline{1}$00] or 1/3[$\underline{1}$100] slip of the upper part of the GaN crystal with respect to the lower part, and are bounded by sessile Frank partial dislocations. By placing a Burgers circuit around the end of the fault one can find that the Frank partial dislocation terminating the BSF has the vector $\boldsymbol{b}$=1/6[2$\underline{2}$03] when a basal plane is removed. The fault with the opposite sign of the Burgers vector $\boldsymbol{b}$=1/6[$\underline{2}$20$\underline{3}$] will appear when a basal plane is inserted. The I$_2$ type BSF with the sequence of …ABAB**ABCA**CACA… was also revealed [Fig. 7(c)]. This type of BSF is necessarily bounded by two glissile Shockley partial dislocations with opposite Burgers vectors ($\boldsymbol{b}$=1/3<1$\underline{1}$00>) [see also Fig. 9(c)].[21]

Figure 7(d) shows an I$_3$ type BSF characterized by the …ABAB**ABCBA**BAB… stacking sequence, where one of the "A" or "B" bilayers is "switched" to the "C" position. This type of fault can also be treated as two I$_1$ BSFs forming a nanotwin of a cubic structure. The incorporation of the first I$_1$ BSF into the wurtzite structure would change the stacking sequence from the original …ABAB… into …BCBC…, but the second I$_1$ BSF would immediately revert the stacking sequence back to the original configuration. It is important to recall the theoretical prediction that only the I$_1$ fault has lower energy than the I$_3$ fault.[15] To the best of our knowledge, the experimental observation of I$_3$ BSF has not been reported elsewhere. We have not observed any termination by partial dislocations for this kind of BSF. These faults are also responsible for the appearance of extra diffraction spots on the [11$\underline{2}$0] zone axis SAED [Fig. 6(b)]. These diffraction spots correspond to a double GaN unit cell in the [0001] direction.

It should be noted at this point that no E type BSFs were observed in this sample. This absence can be ascribed to fact that the formation energy for the E type BSF is higher than that of the other fault types.

C. Prismatic stacking faults

8

Partial dislocations are not the only way to terminate BSFs. Earlier studies[14,16] showed that BSFs can be terminated by PSFs. An example of such termination within the GaN layer is shown in Fig. 4(c). Imaging conditions are set for BSFs to be in a strong contrast. The area "P" between two BSFs has a characteristic contrast of a PSF inclined at some angle to the image plane. These PSFs are visible in edge-on configuration in bright field images obtained for g=11$\underline{2}$0 close to [0001] as thin lines intersecting the sample surface at 60º angle [Fig. 4(d)]. Some of PSFs propagate to the sample surface. Under higher magnification [Fig. 4(e)] it is possible to see that PSFs formed on ($\underline{2}$110) and (1$\underline{2}$10) planes exhibit a zigzag-like structure due to severe faceting on ($\underline{2}$110)/(1$\underline{2}$10) planes. It is assumed that such zigzag-like behavior, which results in an almost vertical propagation of the PSFs from substrate to the sample surface, decreases the total energy of the above PSFs.

In addition to cross-sectional images, PSFs are also revealed in plan-view images. Areas marked by circles in plan-view images [Figs. 5(a,b) and (f,h)] represent PSFs formed on ($\underline{2}$110) and (1$\underline{2}$10) planes intersecting the sample surface at a 60º angle. The estimated density of the PSFs from plan-view bright field images is ~1.8×10^8cm^{-2}. Each of their boundaries in c-planes acts as a termination or nucleation site for a basal stacking fault [Fig. 5(a)]. The separation between two BSFs terminated at a ($\underline{2}$110) or (1$\underline{2}$10) PSFs usually does not exceed 6nm - 7nm, which gives us the characteristic size of a PSF in the [0001] direction.

A characteristic high resolution image of a ($\underline{2}$110) PSF obtained near the Scherzer defocus is shown on Fig. 8(a). In order to determine the atomic structure of the defect experimental and simulated HREM images were compared. Two models, one of a prismatic stacking fault (PSF) [Fig. 2(a)] and one of a stacking mismatch boundary (SMB) [Fig.2(b)], were calculated. Since size of PSFs in the [0001] direction does not exceed 6nm - 7nm, as was measured from plan-view images, simulations were done near Scherzer defocus for sample thicknesses up to 7nm. Simulated HREM images of PSF and SMB calculated for

defocus of -45nm and sample thickness of 4.7nm are shown in Fig. 8(b) and Fig. 8(c), respectively. The simulated image [Fig. 8(b)] of PSF shown on Fig. 2(a) has the closest match to the experimental HREM image shown on Fig. 8(a). The same model of PSF (earlier proposed by Drum[16]) was calculated by Northrup[19] who showed that the PSF is energetically more favorable than the SMB.

A HREM image of a PSF formed on ($\underline{2}$110) or (1$\underline{2}$10) planes intersecting the (11$\underline{2}$0) sample surface at a 60º angle is shown in Fig. 9(a). The inclined defect reveals itself in hexagonal-like contrast [Fig. 9(b)] extending over approximately six (1$\underline{1}$00) interplanar distances between two I_1 type BSFs [the area marked by a dashed box on Fig. 9(a)]. We arbitrarily assigned …ABAB…, as the perfect hexagonal stacking sequence, to atomic columns to the left and to the right sides of the PSF at the bottom part of the image, where the undisturbed structure is revealed [see the assigned letters on both sides of Fig. 9(a)]. As soon as the first I_1 type BSF is introduced it changes the perfect stacking to …ACAC… [left hand side of Fig. 9(a)]. This stacking sequence is kept in the region between two I_1 type BSFs bounding the PSF. To the left side of the PSF there is an …ACAC… sequence, while the stacking sequence to the right of the same defect is …ABAB…. This is an indication of a 1/2[0001] shift between the left and the right parts of the crystal separated by the PSF characterized by a displacement vector R=1/2<10$\underline{1}$1> [see Fig. 2(a), Fig. 8(a) and Fig. 8(b)].

In order to calculate the contrast on a HREM image produced by such a defect image simulations have been carried out using super cells of an inclined PSF lying at a 60º angle to the (11$\underline{2}$0) sample surface plane [Fig. 10(a)]. Due to a shift between the upper and the lower part of the crystal separated by the PSF, atoms in the overlaying region are projected in a hexagonal-like way, which gives rise to a hexagonal-like contrast visible on the simulated HREM image [Fig. 10(b)] calculated with a defocus value of -57.5nm and foil thickness of 3nm. This correlates well

with the experimental image shown on Fig. 9(a). The foil thickness on this experimental HREM image can be estimated from a simple geometry as

$$t = x \cdot tg(60^o) \qquad (1),$$

where x is the PSF projection width on the (11$\underline{2}$0) plane. As mentioned earlier, the PSF projection width extends over approximately six (1$\underline{1}$00) interplanar distances. Inserting $x=6 \cdot d_{1\underline{1}00}$, where $d_{1\underline{1}00}$=0.28nm is the lattice interplanal distance in the [1$\underline{1}$00] direction, into equation (1) we obtain $t = 2.9$nm for the experimental sample thickness.

The same type of hexagonal-like contrast is revealed between two I$_1$ BSFs on Fig. 9(c). The area of the inclined PSF is marked by a dashed box and shown magnified on Fig. 9(d) with superimposed hexagon illustrating hexagonal-like behavior of the observed contrast. Note, that the Shockley partial dislocation shown on the Fig. 9(c) terminates the I$_2$ type BSF. Another Shockley partial with the opposite Burgers vector terminates the I$_2$ somewhere on the right outside the image frame.

D. Stair-rod dislocations

Since the displacement vectors of I$_1$ BSF and PSF are not the same, a stair-rod dislocation is expected at the intersection of these two faults. Furthermore, the I$_1$ BSF can have any one of the possible 1/3<1$\underline{1}$00> displacement vector that alters the stacking sequence of the lattice.

Figure 9(a) shows a plan-view HREM image of a PSF terminated by two I$_1$ BSFs. As it was shown earlier the presence of the inclined PSF, which comes to the (11$\underline{2}$0) sample surface at a 60° angle, reveals itself in a hexagonal-like contrast at the center of the image outlined by the dashed box. Let us assume that of the possible two sets of planes, namely (1$\underline{2}$10) and ($\underline{2}$110), PSF formed on the (1$\underline{2}$10) plane. Then the displacement vector for this PSF will be 1/2[10$\underline{1}$1]. Following the HREM lattice image on Fig. 9(a) from the bottom to the top, it is seen that the stacking sequence begins as ...ABAB... below the PSF. Past the first I$_1$ boundary the sequence

changes to ...CACA within the region spanning the PSF [marked on the left hand side on Fig. 9(a) – compare to the sequence on the right hand side]. The difference between an I_1 displacement vector $1/6[20\underline{2}3]$ and the PSF displacement vector $1/2[10\underline{1}1]$ forms the Burgers vector $b=1/6[10\underline{1}0]$ for the stair-rod dislocation in the screw orientation. That is,

$$1/2[10\underline{1}1] = 1/6[20\underline{2}3] + 1/6[10\underline{1}0].$$

Moving past the second I_1 boundary and above the PSF, the lattice image follows the ...BCBC... stacking sequence [Fig. 9(a)]. In order to change the …CACA… sequence into the …BCBC…, the displacement vector for the second I_1 BSF has to be $1/6[0\underline{2}23]$. Then the stair-rod dislocation at the intersection of the PSF with $R=1/2[10\underline{1}0]$ with the second I_1 ($1/6[0\underline{2}23]$) should be $1/6[3\underline{2}10]$. This stair-rod dislocation will fulfill the equation

$$1/2[10\underline{1}1] = 1/6[0\underline{2}23] + 1/6[3\underline{2}10].$$

This stair-rod has mixed character with $1/6[10\underline{1}0]$ screw and $1/6[2\underline{2}00]$ edge components. The $1/3[1\underline{1}00]$ edge component is responsible for accommodation of different sequences above the PSF.

This, however, is not necessarily the case. There is another possibility when the two I_1 BSFs have displacement vectors that are equal and opposite, so that no net displacement results from the presence of two such I_1 BSFs bounding the PSF. This case corresponds to Fig. 9(c), where stacking sequence is preserved. Although the initial ...ABAB... stacking sequence changes to ...CACA... when crossing the first I_1 boundary, the second I_1 boundary returns the initial ...ABAB... stacking sequence [compare stacking sequences on the left hand side and on the right hand side of the micrograph]. In this case we can write equations for displacement vectors at first and second I_1 boundaries as

$$1/2[10\underline{1}1] = 1/6[20\underline{2}3] + 1/6[10\underline{1}0], \text{ and}$$

$$1/2[10\underline{1}1] = 1/6[\underline{2}023] + 1/6[50\underline{5}0], \text{ respectively.}$$

The displacement vector 1/6[50$\underline{5}$0] of the stair-rod is equivalent to the 1/6[$\underline{1}$010]. A schematic representation of termination of two I_1 BSFs is illustrated on Fig. 9(e), where "s" and "–s" represent 1/6[10$\underline{1}$0] and 1/6[$\underline{1}$010] stair-rod dislocations, respectively.

E. Stacking fault energy

As was mentioned earlier, an I_2 type BSF can be formed either by shear of the crystal in a basal plane by 1/3<1$\underline{1}$00> or by dissociation of a perfect dislocation into two Shockley partials. Fig. 11 shows a high resolution image of the I_2 BSF, which is formed by dissociation of a 1/3<11$\underline{2}$0> perfect dislocation into two Shockley partials with **b**=1/3<1$\underline{1}$00>. Positions of these partials are marked by arrows. The distance between the partials is approximately 5.5nm. The right partial does not give a contrast from the inserted plane on this image since it has only a small component of the Burgers vector projected on the (11$\underline{2}$0) viewing plane. A Burgers circuit placed around the I_2 BSF [marked on Fig. 11 by white countor] shows the fault vector **b**=1/2[1$\underline{1}$00]. The I_1 type BSF also visible on the image extends through the whole field of view and does not alternate the circuit closure failure.

Taking the distance between dissociated dislocations and knowing the elastic constants of the crystal it is possible to estimate the formation energy of the I_2 intrinsic BSF.[13] There is a range of shear moduli μ available in the literature determined by different methods.[22-26] We used several values of μ, such as 24.1 GPa determined by X-ray measurements[22] , 105 GPa, as an average from[23-25] measured by Brillouin scattering, and 81.4 GPa measured by resonant ultrasonic spectroscopy[26]. For the above mentioned values of μ the calculated energies γ were (11.8 ± 1.2) erg/cm^2, (52 ± 5) erg/cm^2, and (40 ± 4) erg/cm^2, respectively. Errors in parentheses reflect the uncertainty in determining the exact positions of the right partial dislocations. The calculated energy of 40 erg/cm^2 is very close to the value of ~ 41 erg/cm^2 and ~ 43 erg/cm^2 obtained theoretically by A. F. Wright[27] and by C. Stampfl

and C. G. Van de Walle.[15] These authors also suggested that stacking fault energy of other nitrides should be higher: ~ 80 erg/cm^2 in InN and ~ 213 erg/cm^2 in AlN[27], or ~ 65 erg/cm^2 in InN and ~ 204 erg/cm^2 in AlN[15].

We were unable to find other reports of stacking fault energy determined experimentally for GaN, but for InN and AlN these energies were (41 ± 8) erg/cm^2 and (220 ± 70) erg/cm^2, respectively[28]. These values were obtained based on the same measurements of dislocation dissociation as in our work. Our stacking fault formation energy value of (40 ± 4) erg/cm^2 for GaN was calculated based on μ = 81.4 GPa. It is the best fit to the experimental values in the series of nitrides: GaN; InN; AlN, and agrees well with theoretical predictions.

V. CONCLUSIONS

Structural defects in nonpolar a-plane GaN grown on a 4H-SiC substrate with an AlN buffer layer have been studied by transmission electron microscopy. Specimens in plan-view and cross-section configuration revealed that the majority of defects are basal and prismatic stacking faults. The majority of basal stacking faults were formed at the 4H-SiC/AlN interface and propagated into the GaN layer. Only low-energy I_1, I_2 and I_3 types of basal stacking faults with a density of ~1.6×10^6cm^{-1} were observed in the GaN layers. Stacking faults of I_1 and I_2 types were terminated by sessile Frank-Shockley and glissile Shockley partial dislocations with Burgers vectors b=1/6<2$\underline{2}$03> and b=1/3<1$\underline{1}$00>. The densities of these partial dislocations at the surface of the GaN layer were ~4.0×10^{10}cm^{-2} and ~0.4×10^{10}cm^{-2}, respectively. For the first time I_3 basal stacking faults were observed experimentally. Based on the high resolution image simulations of prismatic stacking faults we were able to show their formation on (1$\underline{2}$10) or ($\underline{2}$110) planes of GaN. These simulations also confirmed the atomic model for prismatic stacking faults proposed earlier by Drum.[17] Since this defect has a very large fault energy it dissociates into two low-energy I_1 basal

stacking faults with accommodation of the difference between fault vectors at each of two BSF/PSF intersections by a stair-rod dislocation. Separation of Shockley partial dislocations was used to estimate the stacking fault energy for the I_2 type defect in GaN. The estimated value was observed to be in good agreement with theoretical calculations and experimentally determined values for different nitrides.

ACKNOLEDGMENTS

REFERENCES

[1]   S. Nakamura, Science **281**, 956 (1998).

[2]   M. A. Khan, J. W. Yang, G. Simin, R. Gaska, M. S. Shur, and A. D. Bykhovski, Applied Physics Letters **75**, 2806 (1999).

[3]   T. Nishida and N. Kobayashi, Physica Status Solidi A **188**, 113 (2001).

[4]   F. Bernardini and V. Fiorentini, Physical Review B-Condensed Matter **57**, R9427 (1998).

[5]   I. Jin Seo, H. Kollmer, J. Off, A. Sohmer, F. Scholz, and A. Hangleiter, Physical Review B-Condensed Matter **57**, R9435 (1998).

[6]   T. Deguchi, K. Sekiguchi, A. Nakamura, T. Sota, R. Matsuo, S. Chichibu, and S. Nakamura, Japanese Journal of Applied Physics Part 2-Letters **38**, L914 (1999).

[7]   P. Waltereit, O. Brandt, A. Trampert, H. T. Grahn, J. Menniger, M. Ramsteiner, M. Reiche, and K. H. Ploog, Nature **406**, 865 (2000).

[8]   E. Kuokstis, C. Q. Chen, M. E. Gaevski, W. H. Sun, J. W. Yang, G. Simin, M. Asif Khan, H. P. Maruska, D. W. Hill, M. C. Chou, J. J. Gallagher, and B. Chai, Applied Physics Letters **81**, 4130 (2002).

[9]   H. M. Ng, Applied Physics Letters **80**, 4369 (2002).

[10]   M. D. Craven, P. Waltereit, W. Feng, J. S. Speck, and S. P. DenBaars, Japanese Journal of Applied Physics Part 2-Letters **42**, L235 (2003).

[11]   B. A. Haskell, F. Wu, S. Matsuda, M. D. Craven, P. T. Fini, S. P. DenBaars, J. S. Speck, and S. Nakamura, Applied Physics Letters **83**, 1554 (2003).

[12]   J. Jasinski, Z. Liliental-Weber, H. P. Maruska, B. H. Chai, D. W. Hill, M. M. C. Chou, J. J. Gallagher, and S. Brown, Mater. Res. Soc. Symposium Proceedings **764**, 369 (2003).

[13]   D. Hull and D. J. Bacon, *Introduction to Dislocation* (Pergamon Press, Oxford, New York, Beijing, Frankfurt, Sao Paulo, Sydney, Tokyo, Toronto, 1984).

[14] H. Blank, P. Delavignette, R. Gevers, and A. Amelinckx, Physica Status Solidi **7**, 747 (1964).

[15] C. Stampfl and C. G. Van de Walle, Physical Review B-Condensed Matter **57**, R15052 (1998).

[16] C. M. Drum, Philosophical Magazine **11**, 313 (1965).

[17] P. Vermaut, G. Nouet, and P. Ruterana, Applied Physics Letters **74**, 694 (1999).

[18] P. Ruterana, B. Barbaray, A. Bere, P. Vermaut, A. Hairie, E. Paumier, G. Nouet, A. Salvador, A. Botchkarev, and H. Morkoc, Physical Review B-Condensed Matter **59**, 15917 (1999).

[19] J. E. Northrup, Applied Physics Letters **72**, 2316 (1998).

[20] (Programs are available from http://www.totalresolution.com/.

[21] V. Potin, P. Ruterana, and G. Nouet, Journal of Physics-Condensed Matter **12**, 10301 (2000).

[22] V. A. Savastenko and A. U. Sheleg, Physica Status Solidi A **48**, K135 (1978).

[23] Y. Takagi, M. Ahart, T. Azuhata, T. Sota, K. Suzuki, and S. Nakamura, Physica B **219&220**, 547 (1996).

[24] A. Polian, M. Grimsditch, and I. Grzegory, Journal of Applied Physics **79**, 3343 (1996).

[25] M. Yamaguchi, T. Yagi, T. Azuhata, T. Sota, K. Suzuki, S. Chichibu, and S. Nakamura, Journal of Physics-Condensed Matter **9**, 241 (1997).

[26] R. B. Schwarz, K. Khachaturyan, and E. R. Weber, Applied Physics Letters **70**, 1122 (1997).

[27] A. F. Wright, Journal of Applied Physics **82**, 5259 (1997).

[28] K. Suzuki, M. Ichihara, and S. Takeuchi, Japanese Journal of Applied Physics Part 1-Regular Papers Short Notes & Review Papers **33**, 1114 (1994).

FIGURES CAPTION

Fig.1. Atomic models of basal stacking faults (BSFs) in the wurtzite structure projected onto the $(11\underline{2}0)$ plane: (a) I_1 type, (b) I_2 type, (c) E type (d) I_3 type. Stacking sequences are indicated. Large and small circles represent Ga and N atoms, respectively.

Fig.2. Atomic models of (a) a $(1\underline{2}10)$ prismatic stacking fault (PSF) and (b) a $(1\underline{2}10)$ stacking mismatch boundary (SMB) in wurtzite GaN projected onto the (0001) plane. White and black circles represent Ga atoms. Nitrogen atoms are omitted, because their projection would overlap with Ga atoms.

Fig.3. Selected area electron diffraction pattern recorded from a cross-section sample along $[1\underline{1}00]$, showing the epitaxial relationship between GaN layer and the SiC substrate.

Fig.4. Cross-section TEM images: (a) Bright field image ($\boldsymbol{g}=11\underline{2}0$) showing distribution of dislocations with Burgers vector components parallel to $[11\underline{2}0]$. (b) Dark field image ($\boldsymbol{g}=\underline{1}010$) showing that basal stacking faults nucleate at the 4H-SiC/AlN interface and propagate through the GaN to the sample surface. A crack formed approximately 100nm from the AlN buffer layer is marked by an arrow. (c) Bright field image ($\boldsymbol{g}=\underline{1}010$) of an inclined prismatic stacking fault (P) bounded by two basal stacking faults. (d) Bright field image ($\boldsymbol{g}=11\underline{2}0$) taken close to the $[0001]$ zone axis. Prismatic stacking faults formed in $(\underline{2}110)$ or $(1\underline{2}10)$ are visible as thin lines coming to the sample surface at a 60º angle. (e) Higher magnification image recorded under many beam condition showing zigzag-like behavior of a prismatic stacking fault, which results in an almost vertical propagation of the latter from substrate to the sample surface.

Fig.5. Bright field TEM images of a plan-view sample obtained with two perpendicular g-vectors: (a) $g=1\underline{1}00$; parallel lines represent stacking faults formed on the basal plane of GaN. (b) $g=0002$; partial dislocations having a nonzero [0001] component which terminate stacking faults are visible. Small black and white arrows on both images show corresponding places of basal stacking faults terminations by dislocations. Black arrows point to sessile Frank partials dislocations whereas white arrows point to glissile Shockley partials. Areas exhibiting a contrast from inclined prismatic stacking faults are marked by circles. Boundaries of these prismatic stacking faults serve as termination sites for basal stacking faults. Local bending of the GaN layer causes changes in contrast across the images. (c)-(d) Enlargements of (a). (f)-(h) Enlargements of (b).

Fig.6. (a) Selected area electron diffraction pattern recorded from a plan-view sample along the [11$\underline{2}$0] zone axis. Streaking of diffraction spots in [0001] direction arises due to the large number of basal stacking faults. (b) Enlarged part of the diffraction pattern showing additional spots arising from doubled c unit lattice of GaN (marked by white arrows).

Fig.7. High resolution images of a plan-view sample showing typical basal stacking faults observed: (a) Removal of basal plane followed by 1/3[1$\underline{1}$00] slip generates the I_1 basal stacking fault bounded by a sessile Frank partial dislocation with the Burger vector $b=1/6[2\underline{2}03]$. (b) Insertion of an extra basal plane also results in generation of the low-energy I_1 basal stacking fault bounded by a sessile Frank partial dislocation with $b=1/6[2\underline{2}0\underline{3}]$. (c) Shear displacement in the [1$\underline{1}$00] direction leads to formation of the I_2 basal stacking fault, which is bounded by a glissile Shockley partial dislocation. (d) "Switching" of "A" or "B" bilayer to the "C" position results in formation of the I_3 basal stacking fault. Stacking sequences for each basal stacking fault is shown at the left.

Fig.8. (a) High resolution image recorded down to the $[0001]_{GaN}$ zone axis of a prismatic stacking fault formed in ($\underline{2}$110) or (1$\underline{2}$10). (b, c) High resolution image simulations (defocus -45.0nm; thickness 4.7nm): (b) based on Drum's prismatic stacking fault model [Fig. 2(a)], and (c) based on Amelinkx's stacking mismatch boundary [Fig. 2(b)].

Fig.9. (a) High resolution image of an inclined prismatic stacking fault (PSF) (inside dashed box) projected onto the (11$\underline{2}$0) revealing hexagonal-like contrast. The PFS terminates two I_1 basal stacking faults. Stacking sequences on the right and the left sides of the image show the 1/2[0001] shift induced by the inclined PSF. The first I_1 changes the stacking sequence from …ABAB… to …ACAC…. This sequence is preserved until the second I_1 BSF converts it to …BCBC…. (b) Magnified area inside dashed box in (a). (c) HREM image of PSF, which terminates two I_1 BSFs. Stacking sequences on the right and the left sides are shown. No net displacement in [1$\underline{1}$00] induced by BSFs is observed. Though the initial ...ABAB... stacking sequence changes to ...CACA... when crossing the first I_1 boundary, the second I_1 boundary restores the initial ...ABAB... stacking sequence. A Shockley partial dislocation (1/3<1$\underline{1}$00>), which arises from the termination of I_2 basal stacking fault, is also marked. A second dislocation with opposite Burgers vector is located to the right outside the image frame. (d) Magnified area inside dashed box in (c). (e) Schematic representation of termination of two I_1 BSFs by PSF, "s" and "–s" represent 1/6[10$\underline{1}$0] and 1/6[$\underline{1}$010] stair-rod dislocations.

Fig.10. (a) Drum's atomic model [Fig. 2(a)] of a prismatic stacking fault formed in ($\underline{2}$110) or (1$\underline{2}$10) planes projected onto the (11$\underline{2}$0) plane of GaN. (b) Simulated high resolution image (defocus -57.5nm; thickness 3nm) of inclined prismatic stacking fault based on Drum's models shown in (a).

Fig.11. High resolution image of a dissociated $1/3<11\underline{2}0>$ perfect dislocation into two Shockley partials $(1/3<1\underline{1}00>)$ bounding the I_2 basal stacking fault. Arrows indicate the positions of the partials. The Burgers contour placed around I_2 BSF shows a closure failure equal to $1/2[1\underline{1}00]$. The I_1 BSF, marked outside the contour, extends though all image from the left to the right, and thus does not influence the contour failure.
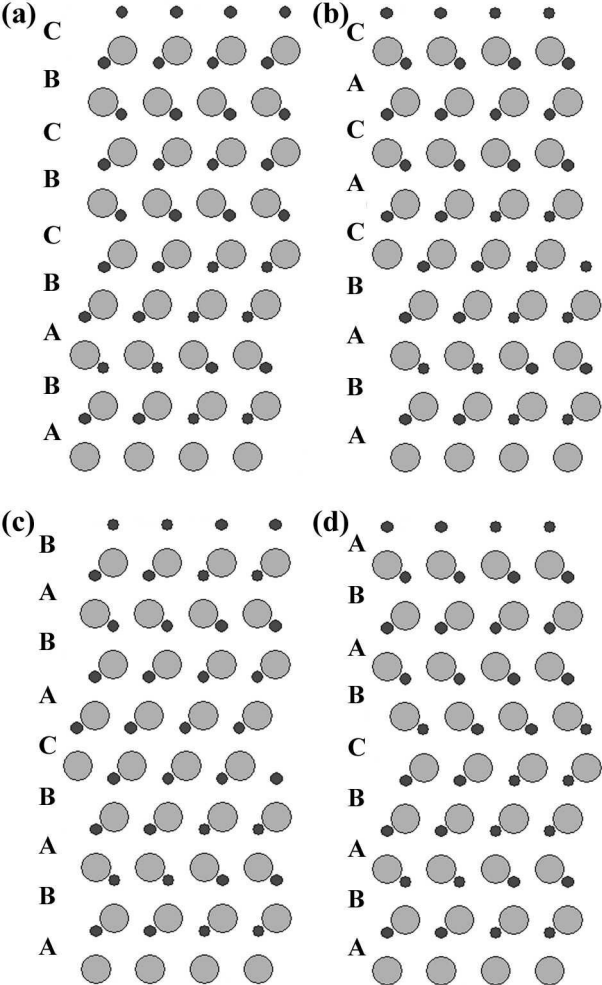
Fig.1
BT9202
Zakharov et al.
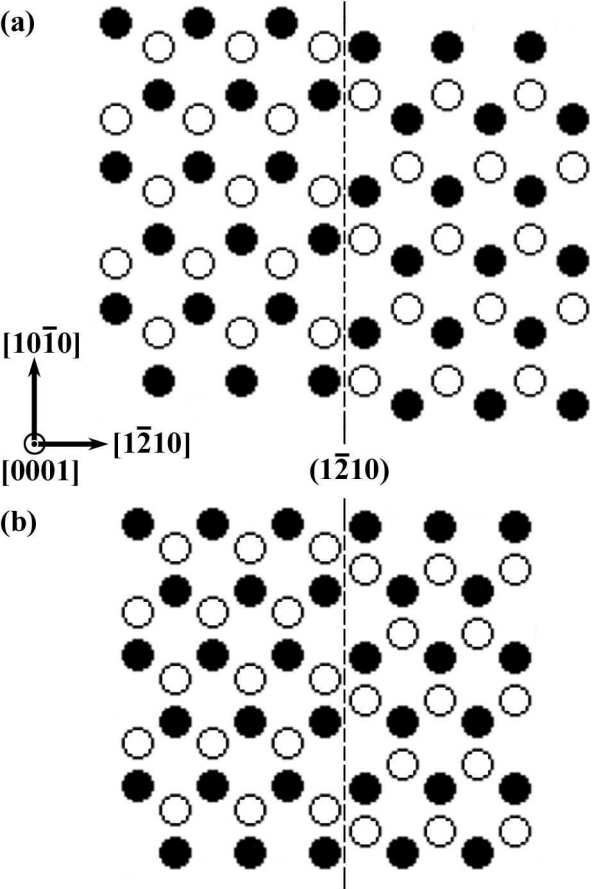
(a)

$[10\bar{1}0]$

$[1\bar{2}10]$

$[0001]$

$(1\bar{2}10)$

(b)

Fig.2
BT9202
Zakharov et al.

Fig.3
BT9202
Zakharov et al.

a — GaN layer, 4H-SiC, AlN, $11\bar{2}0$, 100nm

b — GaN layer, AlN, 4H-SiC, $\bar{1}01\bar{0}$, 100nm

c — P, 10nm

d — GaN layer, AlN, 4H-SiC, $60^0 \lambda \wedge 60^0$, $11\bar{2}0$, 100nm

e — 10nm
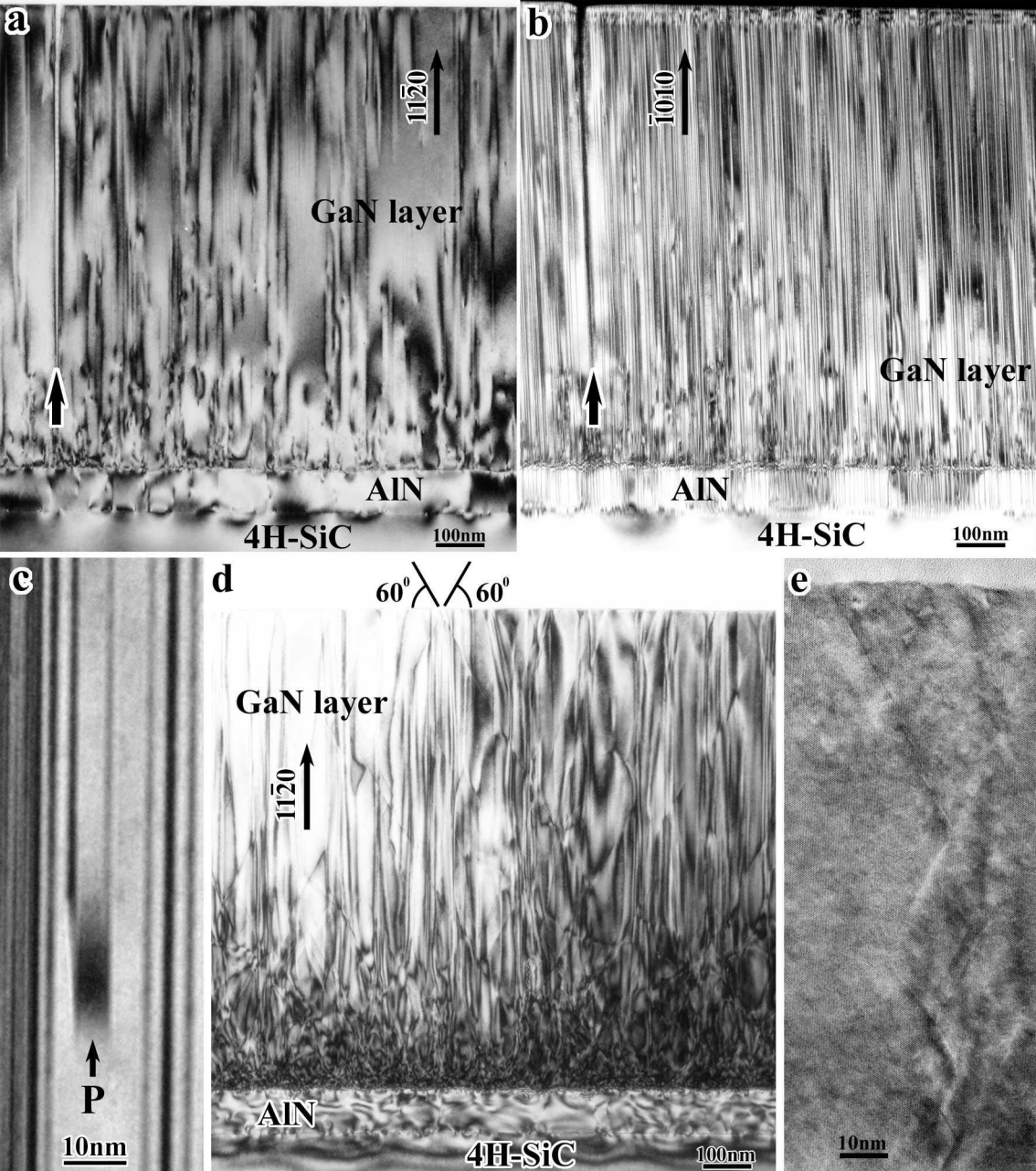
Fig.4
BT9202
Zakharov et al.
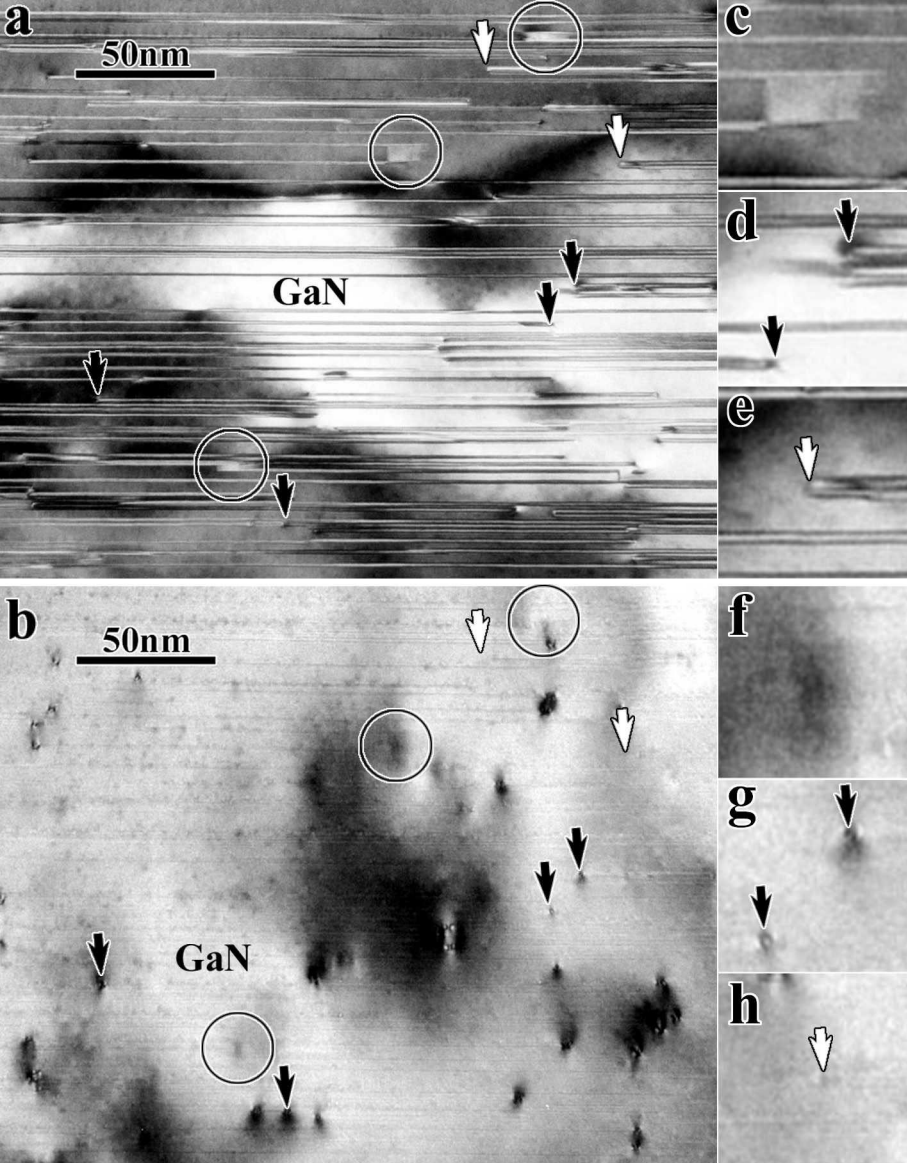
Fig.5
BT9202
Zakharov et al.

(a) [11$\bar{2}$0]

0002

1$\bar{1}$00

(b)
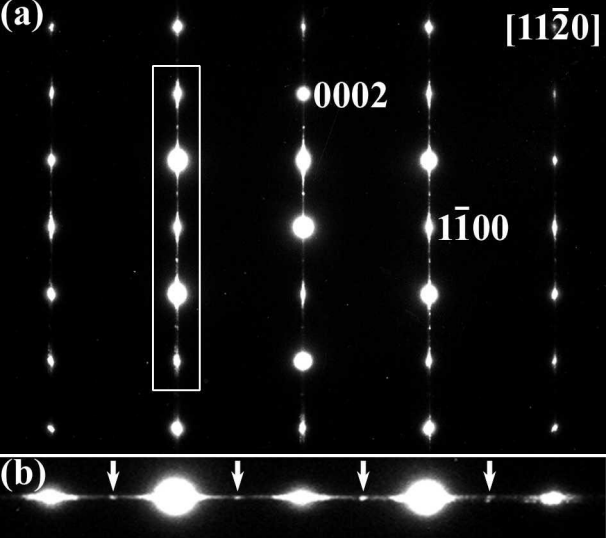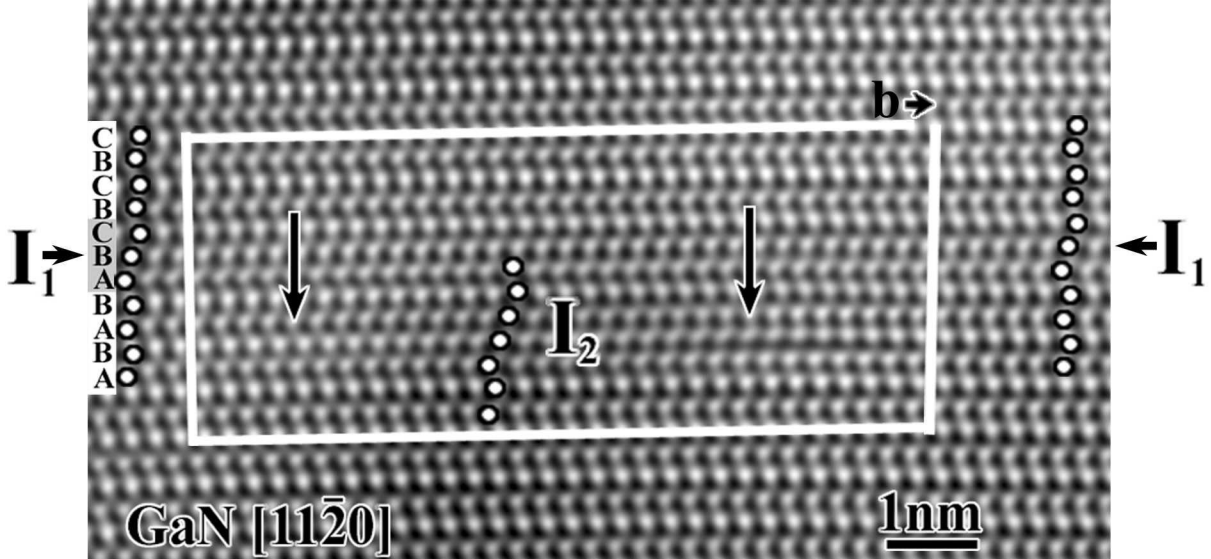
Fig.6
BT9202
Zakharov et al.

Fig.7
BT9202
Zakharov et al.

a

b

c

[10$\bar{1}$0]
or
[0$\bar{1}$10]

[1$\bar{2}$10] or [$\bar{2}$110]

[0001]

Fig.8
BT9202
Zakharov et al.

a GaN [11$\bar{2}$0]

I_1

I_1

1nm

b

c GaN [11$\bar{2}$0]

I_1

I_1

I_2

1nm

d

e

I_1

I_1

90^0

PSF

s

$-s$

60^0

[11$\bar{2}$0]

[1$\bar{1}$00]

[0001]

Fig.9
BT9202
Zakharov et al.

(a)

[0001]

[$\bar{1}$100]

[11$\bar{2}$0]

(b)
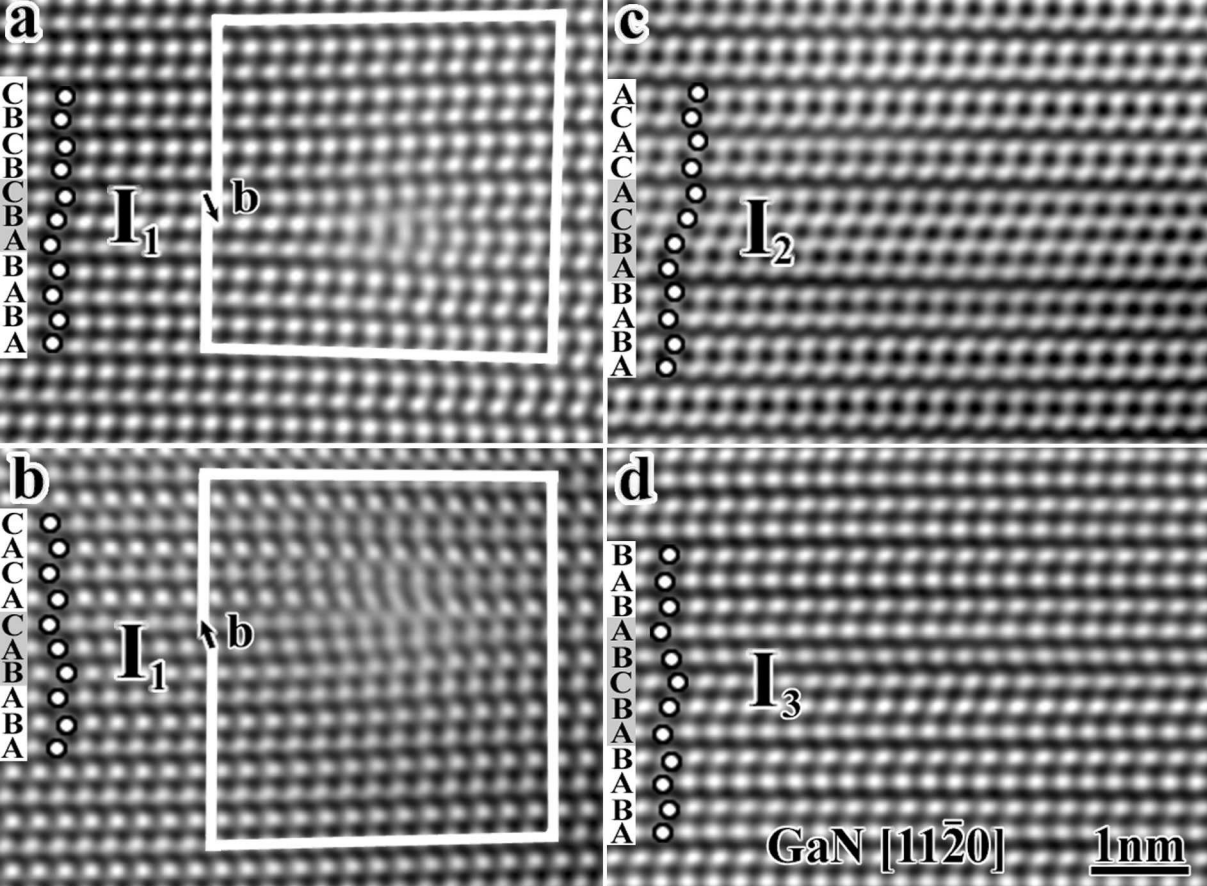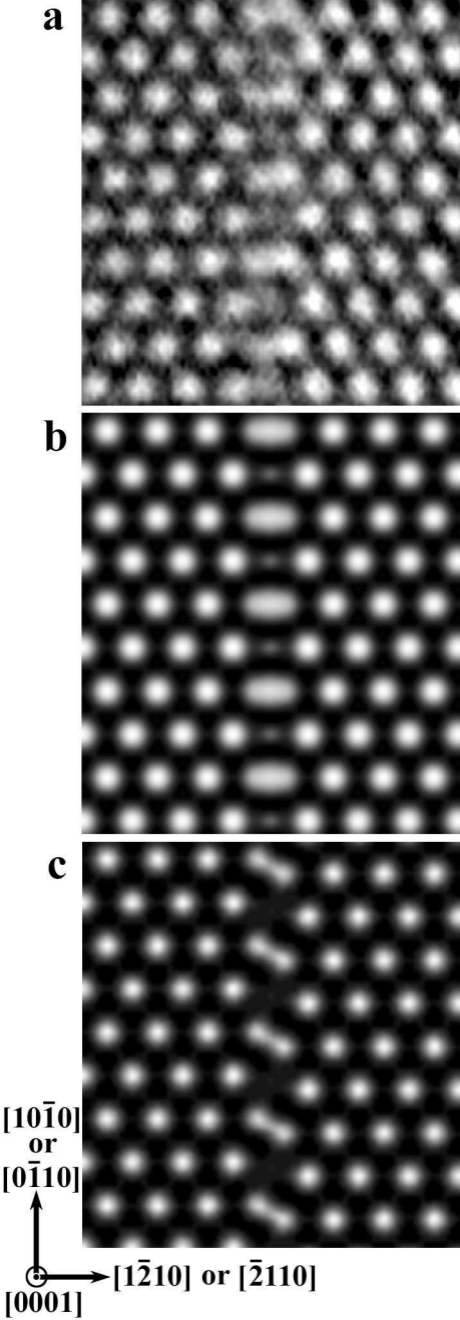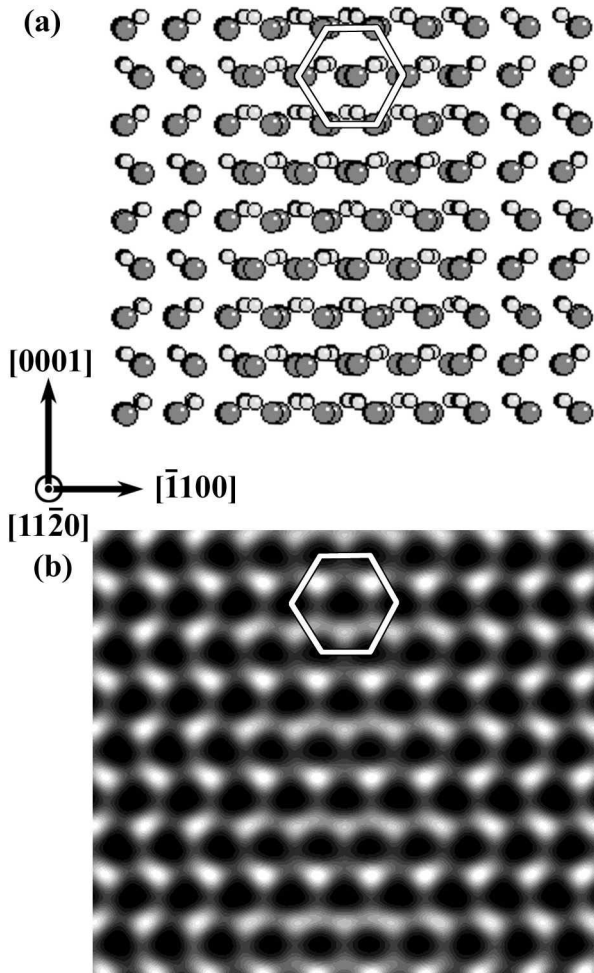
Fig.10
BT9202
Zakharov et al.

Fig.11
BT9202
Zakharov et al.